Molecular Crystals and Liquid Crystals

ISSN: 1542-1406 (Print) 1563-5287 (Online) Journal homepage: http://www.tandfonline.com/loi/gmcl20

Hyperpolarizability, Hirshfeld, and density functional theory computations of a nonlinear optical picrate

R. Agilandeswari, A. Aditya Prasad, S. Sivaraman, S. Kalainathan & SP. Meenakshisundaram

To cite this article: R. Agilandeswari, A. Aditya Prasad, S. Sivaraman, S. Kalainathan & SP. Meenakshisundaram (2016) Hyperpolarizability, Hirshfeld, and density functional theory computations of a nonlinear optical picrate, Molecular Crystals and Liquid Crystals, 625:1, 238-252, DOI: 10.1080/15421406.2015.1069477

To link to this article: http://dx.doi.org/10.1080/15421406.2015.1069477

Published online: 19 Feb 2016.

MOL. CRYST. LIQ. CRYST.
2016, VOL. 625, 238–252
http://dx.doi.org/10.1080/15421406.2015.1069477

Taylor & Francis
Taylor & Francis Group

Hyperpolarizability, Hirshfeld, and density functional theory computations of a nonlinear optical picrate

R. Agilandeswari[a], A. Aditya Prasad[a], S. Sivaraman[a], S. Kalainathan[b], and SP. Meenakshisundaram[a]

[a]Department of Chemistry, Annamalai University, Chidambaram, Tamil Nadu, India; [b]Crystal Research Centre, Vellore Institute of Technology, Vellore, Tamil Nadu, India

ABSTRACT

bis(2-nitroaniline) picrate (BNP) single crystals was grown by slow evaporation growth technique using mixed solvent system with methanol–acetone (1:1, v/v) at a constant temperature, and the structure was interpreted by single crystal X-ray, Power Diffraction (XRD) analysis. Inter- and intramolecular hydrogen bonding interactions were interpreted, and crystal cohesion was architectured by N-H···O, O-H···O, C-H···N, H···H, O···O, and $\pi\cdots\pi$ staking interactions. All intermolecular interactions occurring in the crystal lattice were calculated using fingerprint analysis. Interaction strengths were graphically illustrated by the Hirshfeld surface analysis. The band gap energy of BNP was estimated by the application of the Kubelka–Munk algorithm. Nonlinear optical behavior was confirmed by the Kurtz–Perry technique. Optimized geometry was derived by the density functional theory calculations. The first-order molecular hyperpolarizability (β) and excited state energies were estimated by the time-dependent density functional theory analysis.

KEYWORDS

Band gap; DFT and TD-DFT; fingerprint plots; Hirshfeld surface; polarizability

GRAPHICAL ABSTRACT

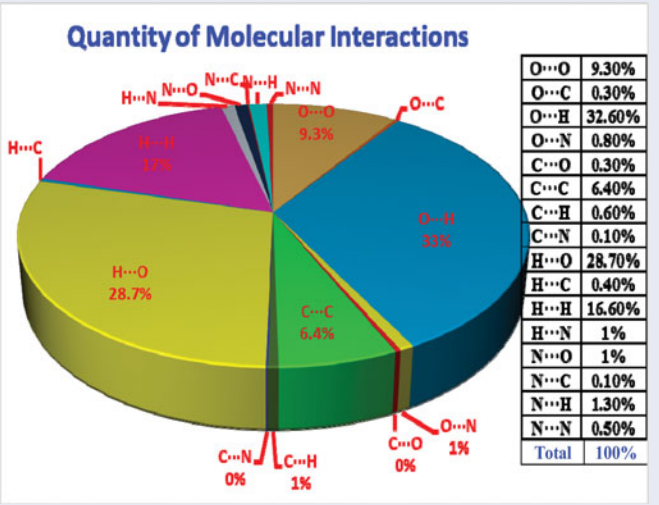

CONTACT SP. Meenakshisundaram meenakshisundaram.sp.294@annamalaiuniversity.ac.in Department of Chemistry, Annamalai University, Chidambaram, Tamil Nadu, India.

Color versions of one or more of the figures in the article can be found online at www.tandfonline.com/gmcl.

1. Introduction

Nonlinear optical (NLO) single crystals are being developed progressively for the past few years as these are essential for the electro-optical field. Optical crystals exhibit several interesting physical properties such as phase transitions, electric, dielectric, ferroelectric, and piezoelectric behavior [1,2]. Organic NLO materials usually possess π-electron-conjugated system with an electron donor group on one end and an acceptor group on the other, which leads to a push–pull conjugated structure, leading to their applications in optical and optoelectronic devices [3,4]. Structural variations due to polymorphic transitions of simulated methodology are investigated earlier [5,6]. Most of the picrates are a family of conjugated NLO chromophores that reveal good second harmonic generation (SHG) and transparency [7,8]. Several complexes of picric acid with organic molecules exhibit NLO applications [9]. Recently, we have investigated the synthesis, structure, growth, and characterization of p-toluidinium picrate [10], 2-amino-5-nitrobenzophenonium picrate [11], 4-aminobenzophenonium picrate [12], and 4-aminopyridinium picrate [13].

In the present work, we report the polymorphic structure, ultraviolet–diffuse reflectance spectroscopy (UV-DRS), fluorescence, density functional theory (DFT) computations of first-order molecular hyperpolarizability, Hirshfeld surface analysis, fingerprint plots, excitation energies, and Mulliken and natural population analysis.

2. Experimental procedure

2.1. *Synthesis and growth*

Bis(2-nitroaniline) picrate (BNP) was synthesized by mixing stoichiometric amounts of 2-nitroaniline (Sigma-Aldrich) and picric acid (Sigma-Aldrich) in the ratio of 2:1 using methanol as A solvent. The mixture was stirred at room temperature for 3 hr and BNP was achieved as a yellow color precipitate. The product was purified by repeated recrystallization processes using mixed solvent: methanol and acetone (1:1, v/v). Recrystallized BNP was dissolved in mixed solvent system (methanol:acetone, 1:1, v/v), and the solution was warmed with constant stirring for an hour to avoid co-precipitation of multiple phases. Transparent crystals were grown by the slow evaporation solution growth technique and the crystals were collected after a period of 10–12 days. Photograph of BNP is displayed in Fig. 1.

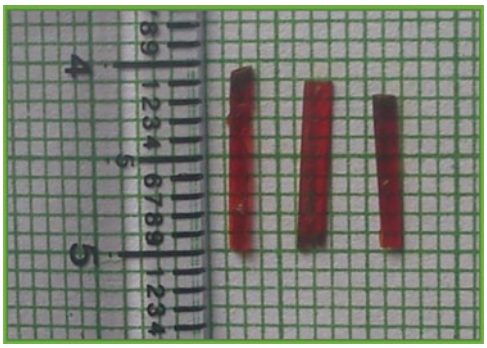

Figure 1. Photograph of BNP crystals.

2.2. *Computational details*

Complete theoretical calculations were performed at density functional theoretical level with B3LYP/6-31G(d, p) as a basis set using Gaussian 09W [14] program package. Images are visualized using the GaussView 5.0 visualization program [15]. The vibrational wavenumbers of normal modes were calculated by total energy distribution (TED) using VEDA 4 package [16]. Excitation energy of the molecule is estimated by time-dependent DFT (TD-DFT), configuration interaction single (CIS), and Zerner's Intermediate Neglect of Differential Overlap (ZINDO) methods. Hirshfeld surfaces and fingerprint plots were generated from the crystal data using the DFT method with 6-31G(d, p) as a basis set [17].

2.3. *Characterization techniques*

The structural analysis of BNP was carried out using Bruker AXS (Kappa APEXII) X-ray diffractometer with Mo-Kα radiation ($\lambda = 0.71073$ Å). The crystal was kept at 293.15 K during data collection. Using Olex2 [18], the structure was solved with the "olex2.solve" [19] structure solution program using charge flipping, and refined with the "olex2.refine" [19] refinement package using the Gauss–Newton minimization. Crystal data for $C_{36}H_{30}N_{14}O_{22}$ ($M = 1010.72$ g mol^{-1}): monoclinic, space group *Cc*, μ(Mo-Kα) $= 0.172$ mm^{-1}, Dcalc $=$ 2.0355 g cm^{-3}, 9444 reflections measured ($5.42° \leq 2\Theta \leq 56.06°$), 3637 unique ($R_{int} = 0.0280$, $R_{sigma} = 0.0294$), which were used in all calculations. The final R_1 was 0.0585 ($I \geq 2u(I)$) and wR_2 was 0.1736 (for all data). NLO property (SHG) of BNP is measured by the Kurtz and Perry technique [20,21]. Electronic absorption spectra were recorded on a Varian Model Cary 100 UV-Vis spectrometer. Diffuse reflectance spectra of the samples were recorded using the DRA-CA-30I. Fluorescence excitation and emission spectra were recorded on a Horiba Jobin Yvon Model FL3-22 Fluorolog spectrofluorimeter. Electrostatic resonance (ESR) spectra were recorded using Bruker-ER073 instrument equipped with an EMX micro-X source for X-band measurement.

3. Results and discussion

3.1. *Optimized geometry*

The optimized molecular structure of BNP is shown in Fig. 2b, and it closely resembles the XRD structure. Fig. 2a represents intramolecular interactions in BNP. Red color lines in contour map (Fig. 2c) indicate high reactive site, and yellow color lines represent very less reactivity.

The atomic charge transfer of the atoms present in BNP is accomplished by the Mulliken population investigation [22,23], presented in Fig. 3, and the analogous charge values are recorded in Table 1. Mulliken atomic charges have an important portion in the application of quantum mechanical calculation to molecular construction. From the detailed atomic charge values, nitrogen (−0.627, −0.814, −0.39, and −0.88 e) and oxygen (v0.745 and −0.792 e) in BNP have a large negative charge and act as electron donors. All hydrogen atoms (0.216, 0.206, 0.229, and 0.387 e), which are acceptor atoms, disclose positive charge, and this might be due to the attachment of extra electronegative atoms. Most of the atomic charges are matched with the natural atomic charges. Minor differences in the natural and Mulliken atomic charges are noted. The variation error between the natural and Mulliken atomic charges has been

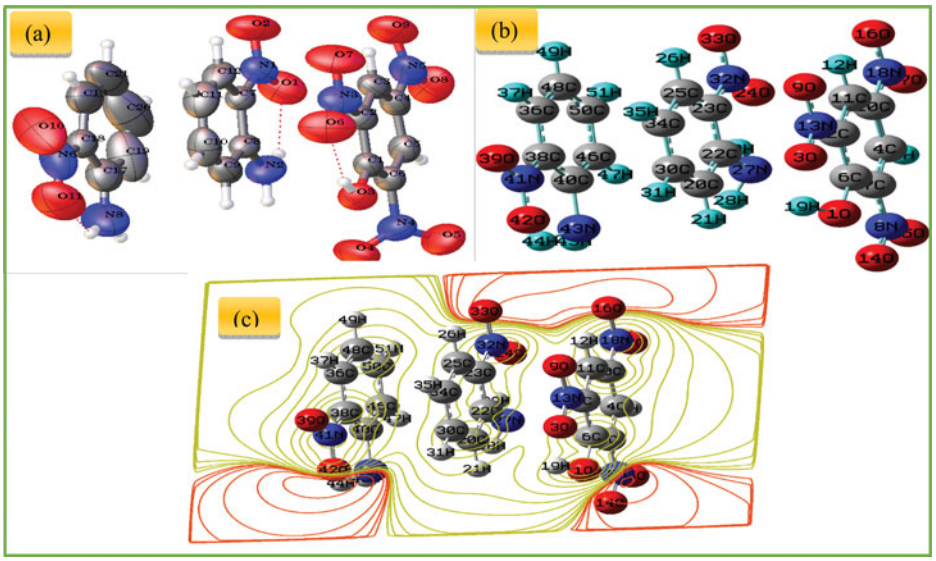

Figure 2. Molecular structure of BNP: (a) Ellipsoid plot. (b) Optimized structure. (c) Contour map.

expressed by root mean square deviation (RMSD) [24,25] using the following expression:

$$\mathrm{RMSD} = \sqrt{\frac{1}{n-1}\sum_{i}^{n}\left(\gamma_i^{\mathrm{Natural}} - \gamma_i^{\mathrm{Mulliken}}\right)^2},$$

where n is the number of natural or Mulliken data. The RMSD value is found to be 0.00001% error for natural and Mulliken atomic charges.

3.2. *Time-dependent DFT analysis*

Absorbance spectrum of BNP illustrate minimum absorption in the visible region. To support experimental observations, the theoretical electronic excitation energies, absorption wavelengths, and oscillator strengths were calculated by TD-DFT methods using GAUSSIAN 09W program with basis set 3-21G by CAMB3LYP method. TD-DFT excitation energy is observed at ~376-nm wavelength, experimentally it is at ~380-nm wavelength (Fig. 4). Excitation energies detected from ZINDO and CIS are ~577 nm and ~305 nm respectively. From this we can conclude that the TD-DFT method is a more reliable method than other methods. Oscillator strengths of TD-DFT, ZINDO, and CIS methods are 0.0309 *f*, 0.0001 *f*, and 0.0002 *f* respectively. Fluorescence emission peak is absolved at a range of ~428-nm wavelength (Fig. 5).

The highest occupied molecular orbital (HOMO) and the lowest unoccupied molecular orbital (LUMO) of BNP are shown in Fig. 6. The frontier orbital gap enables in describing the chemical reactivity and kinetic strength of the molecule. The red and green colors respectively represent the positive and negative standards of wave function. The HOMO is the orbital that primarily perform as an electron donor, and the LUMO is the orbital that mainly acts as an electron acceptor [26,27]. The energy gap between HOMO (–7.215 eV) to LUMO (–4.122 eV) of the molecule is about 3.093 eV. The chemical hardness of the molecule is calculated using

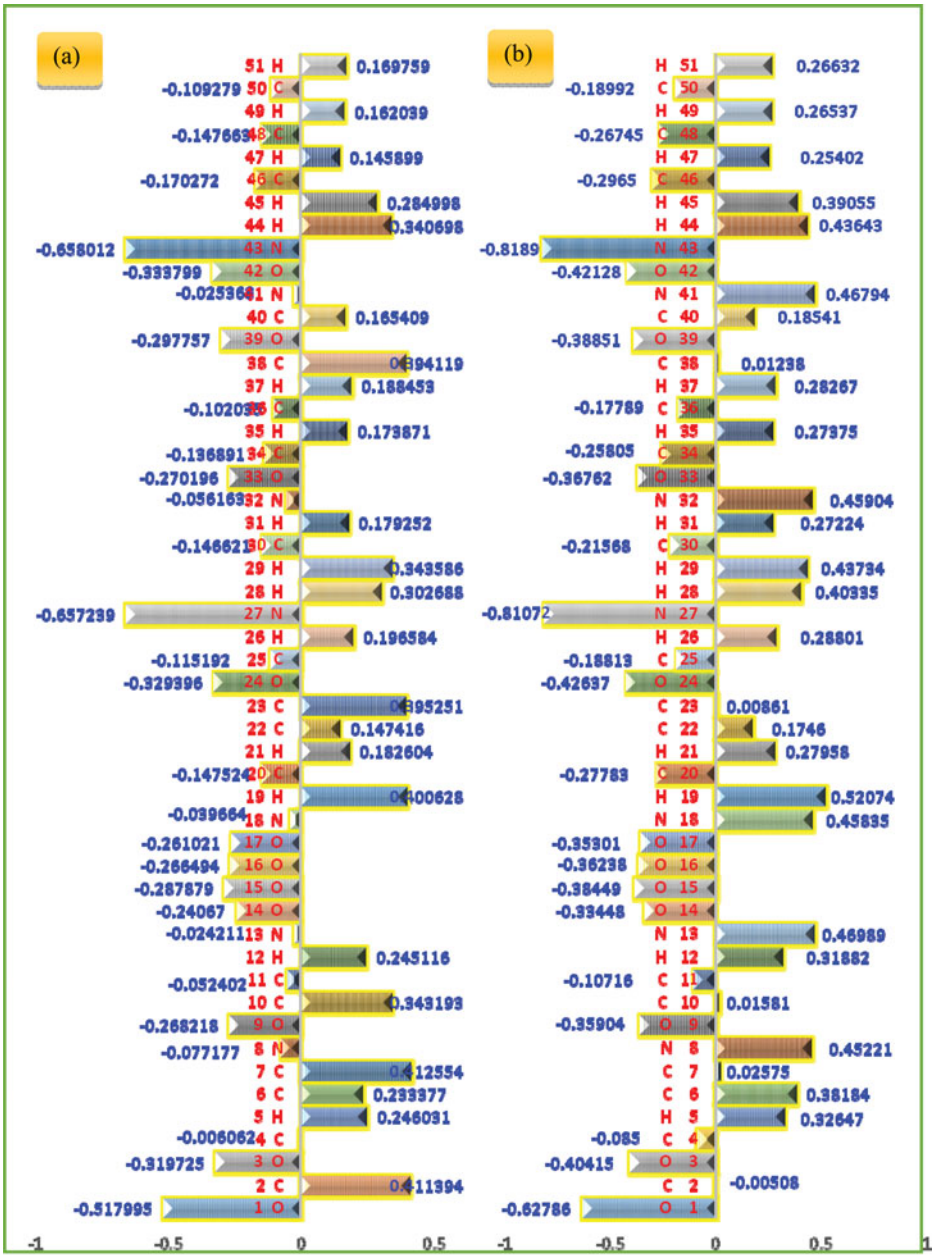

Figure 3. (a) Bar-chart of the Mulliken atomic charges. (b) Bar-chart of natural charges.

the Koopman's theorem [28], and is given by the following expression:

$$\eta = \frac{(\mathrm{IP} - \mathrm{EA})}{2} = 1.5465\,\mathrm{eV}$$

where ionization potential, IP ≈ −E (eV) (HOMO); electron affinity, EA ≈ −E (eV) (LUMO). Owing to chemical hardness, a large HOMO–LUMO gap specifies hardness of molecule, and a small HOMO–LUMO gap specifies softness of molecule. The stability of molecule in the direction of hardness asserts that the molecule with the smallest HOMO–LUMO gap specifies that it is more reactive.

Table 1. Atomic charge population [DFT, 6-31G (d, p)] of BNP.

Mulliken population			Natural Population		
Atom		Charge (e)	Atom		Charge (e)
1	O	− 0.517995	O	1	−0.62786
2	C	0.411394	C	2	−0.00508
3	O	− 0.319725	O	3	−0.40415
4	C	− 0.006062	C	4	−0.085
5	H	0.246031	H	5	0.32647
6	C	0.233377	C	6	0.38184
7	C	0.412554	C	7	0.02575
8	N	− 0.077177	N	8	0.45221
9	O	− 0.268218	O	9	− 0.35904
10	C	0.343193	C	10	0.01581
11	C	− 0.052402	C	11	− 0.10716
12	H	0.245116	H	12	0.31882
13	N	− 0.024211	N	13	0.46989
14	O	− 0.24067	O	14	− 0.33448
15	O	− 0.287879	O	15	− 0.38449
16	O	− 0.266494	O	16	− 0.36238
17	O	− 0.261021	O	17	− 0.35301
18	N	− 0.039664	N	18	0.45835
19	H	0.400628	H	19	0.52074
20	C	− 0.147524	C	20	− 0.27783
21	H	0.182604	H	21	0.27958
22	C	0.147416	C	22	0.1746
23	C	0.395251	C	23	0.00861
24	O	− 0.329396	O	24	− 0.42637
25	C	− 0.115192	C	25	− 0.18813
26	H	0.196584	H	26	0.28801
27	N	− 0.657239	N	27	− 0.81072
28	H	0.302688	H	28	0.40335
29	H	0.343586	H	29	0.43734
30	C	− 0.146621	C	30	− 0.21568
31	H	0.179252	H	31	0.27224
32	N	− 0.056163	N	32	0.45904
33	O	− 0.270196	O	33	− 0.36762
34	C	− 0.136891	C	34	− 0.25805
35	H	0.173871	H	35	0.27375
36	C	− 0.102035	C	36	− 0.17789
37	H	0.188453	H	37	0.28267
38	C	0.394119	C	38	0.01238
39	O	− 0.297757	O	39	− 0.38851
40	C	0.165409	C	40	0.18541
41	N	− 0.025363	N	41	0.46794
42	O	− 0.333799	O	42	− 0.42128
43	N	− 0.658012	N	43	− 0.8189
44	H	0.340698	H	44	0.43643
45	H	0.284998	H	45	0.39055
46	C	− 0.170272	C	46	− 0.2965
47	H	0.145899	H	47	0.25402
48	C	− 0.147663	C	48	− 0.26745
49	H	0.162039	H	49	0.26537
50	C	− 0.109279	C	50	− 0.18992
51	H	0.169759	H	51	0.26632

3.3. *UV-DRS*

The indirect band gap energy (Fig. 7) of crystalline material is calculated as 2.39 eV from reflections of the Tauc plot by the application of the Kubelka–Munk algorithm [29] (theory provides correlation between reflectance and concentration),

$$F(R) = (1 - R)^2/2R = \alpha/s = Ac/s,$$

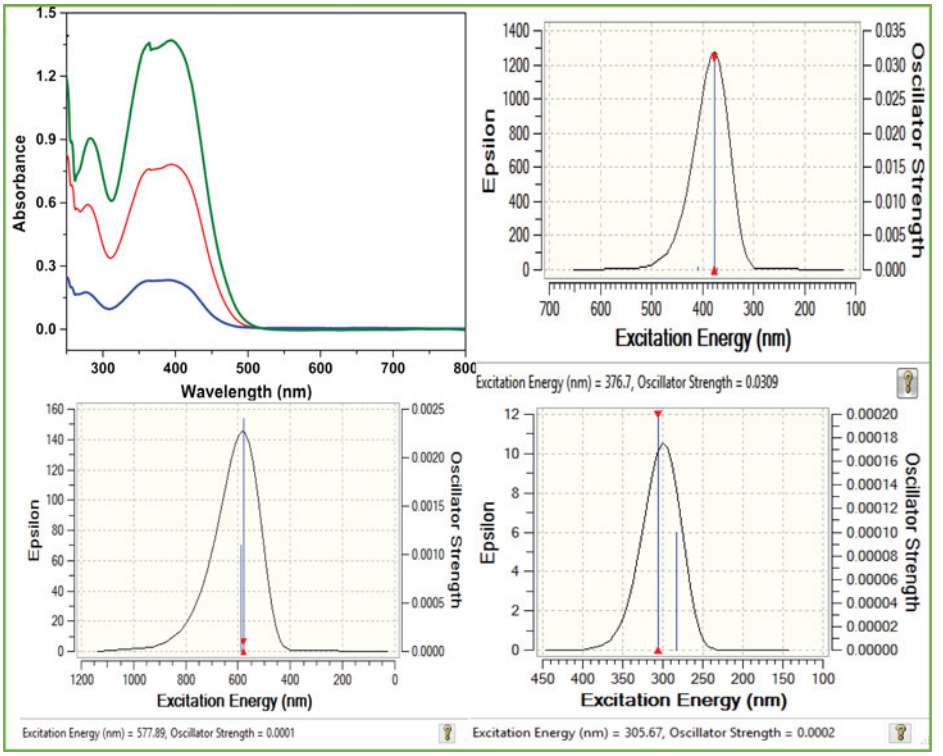

Figure 4. Excitation energy of BNP: (a) Experimental; (b) TD-DFT; (c) ZINDO; and (d) CIS.

where *F(R)* is the Kubelka–Munk function, *R* is the reflectance of the solid, *s* is the scattering coefficient, *A* is the absorbance, and ***c*** is the concentration of the absorbing species.

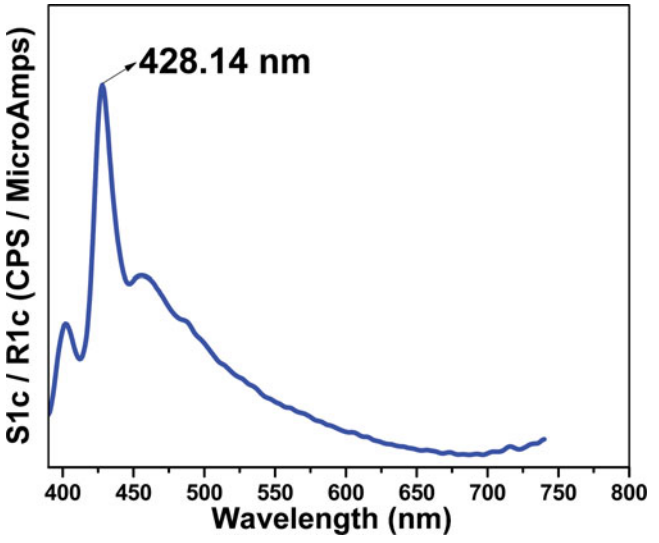

Figure 5. Fluorescence spectra of BNP.

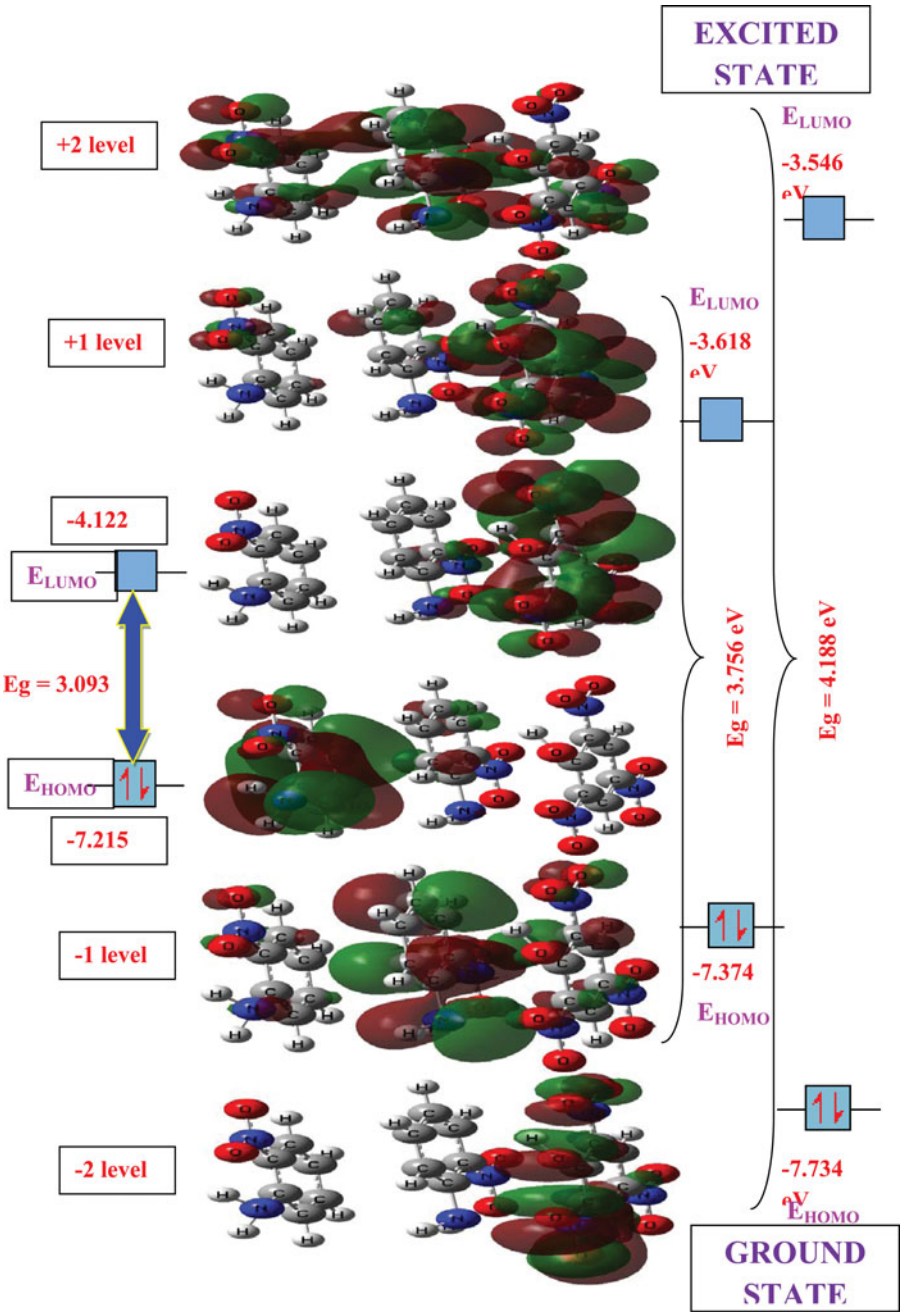

Figure 6. **The** HOMO–LUMO energy gap of BNP.

3.4. *Single crystal XRD*

BNP crystallizes in monoclinic system with non-centrosymmetric space group *Cc* and the cell parameters are $a = 9.304$ Å (3), $b = 14.136$ Å (4), $c = 13.11$ Å (4) and $\beta = 107°$ (4), $V = 1649$ A^3 (9). Cell parameters matches with the earlier structure [30], but structure morphology differs. The crystal cohesion is achieved by N-H···O, O-H···O, C-H···N, H···H, O···O, and $\pi \cdots \pi$ staking interactions. Weak intermolecular interactions play a major role in supramolecular

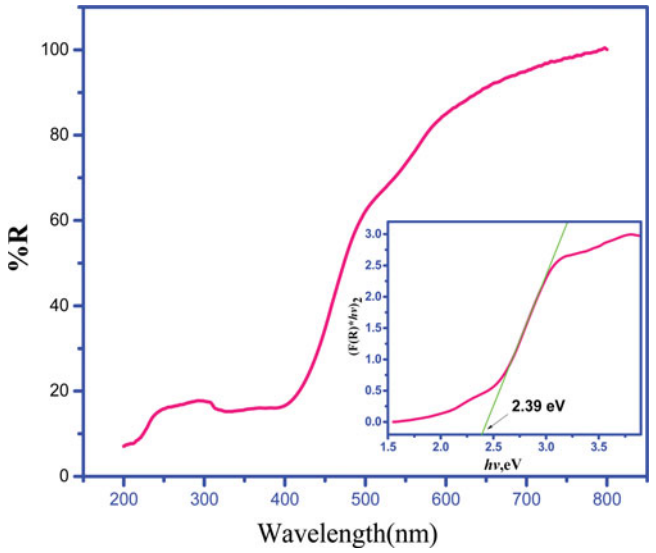

Figure 7. UV-DRS absorbance spectrum of BNP (Tauc plot in inset).

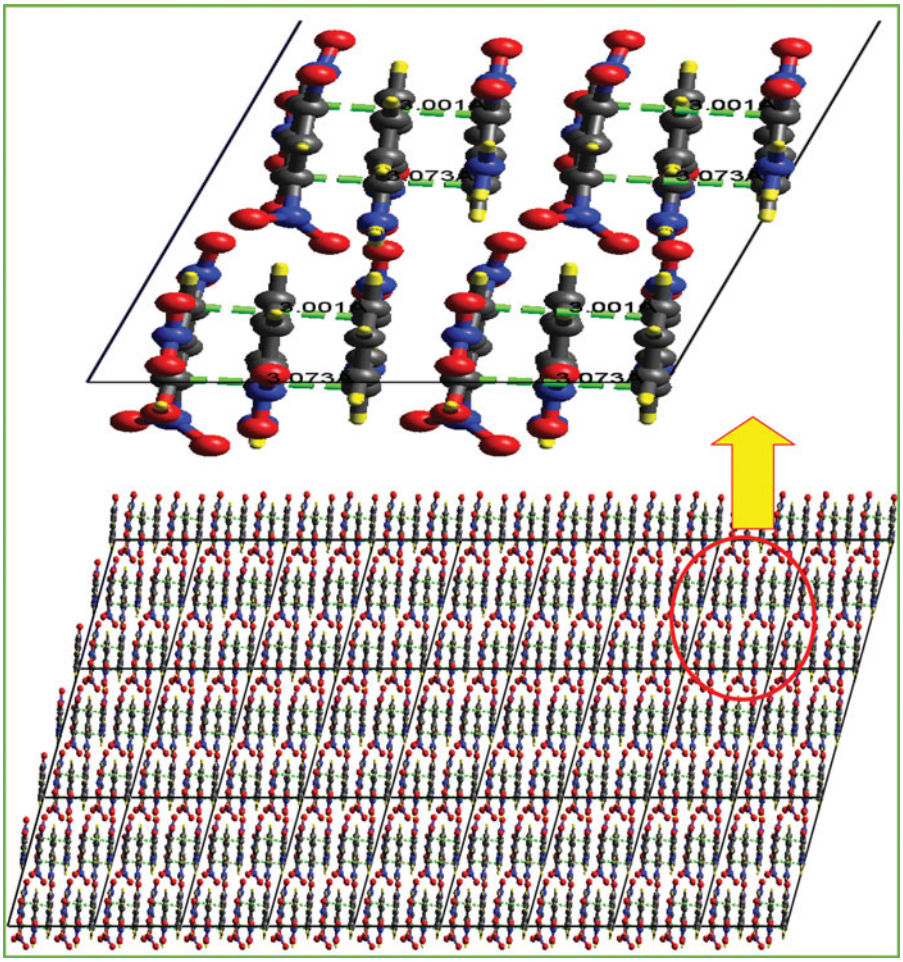

Figure 8. Packing projection along the *a*-axis showing $\pi \cdots \pi$ interactions.

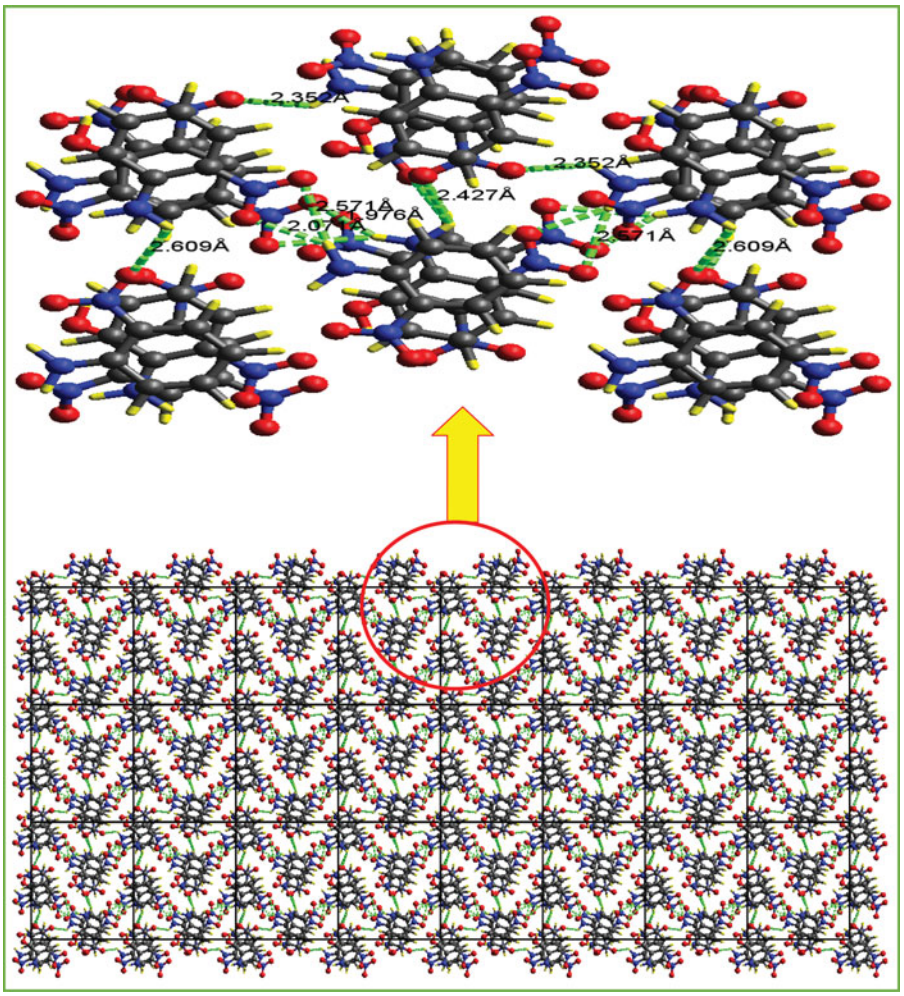

Figure 9. Packing projection along the *b*-axis showing N—H···O interactions.

materials. Weak supramolecular $\pi\cdots\pi$ staking interactions are displayed in Fig. 8, with interaction distances of 3.001 and 3.073 Å. Crystal packing projections formed along the *b*-axis look like zigzag structure. N-H···O (Fig. 9) interactions were assembled with a bond distance of about 1.976, 2.071, 2.352, 2.427, and 2.609 Å. Weak intermolecular contacts are assembled by H···H and O···O (Fig. 10), and these interactions were organized with a distance of about 2.139 and 2.378 Å, and 2.882 and 2.844 Å respectively. The crystallography information is provided in the supplementary data.

3.5. *First-order molecular hyperpolarizability*

The first-order hyperpolarizability is a third-rank tensor that can be described by a 3 × 3 × 3 matrix. The 27 components of 3D matrix can be reduced to 10 components due to the Kleinman symmetry [31]. It can be given in the lower tetrahedral format:

$$E = E_0 - \mu_\alpha F_\alpha - 1/2\alpha_{\alpha\beta}F_\alpha F_\beta - 1/6\beta_{\alpha\beta\gamma}F_\alpha F_\beta F_\gamma + \ldots,$$

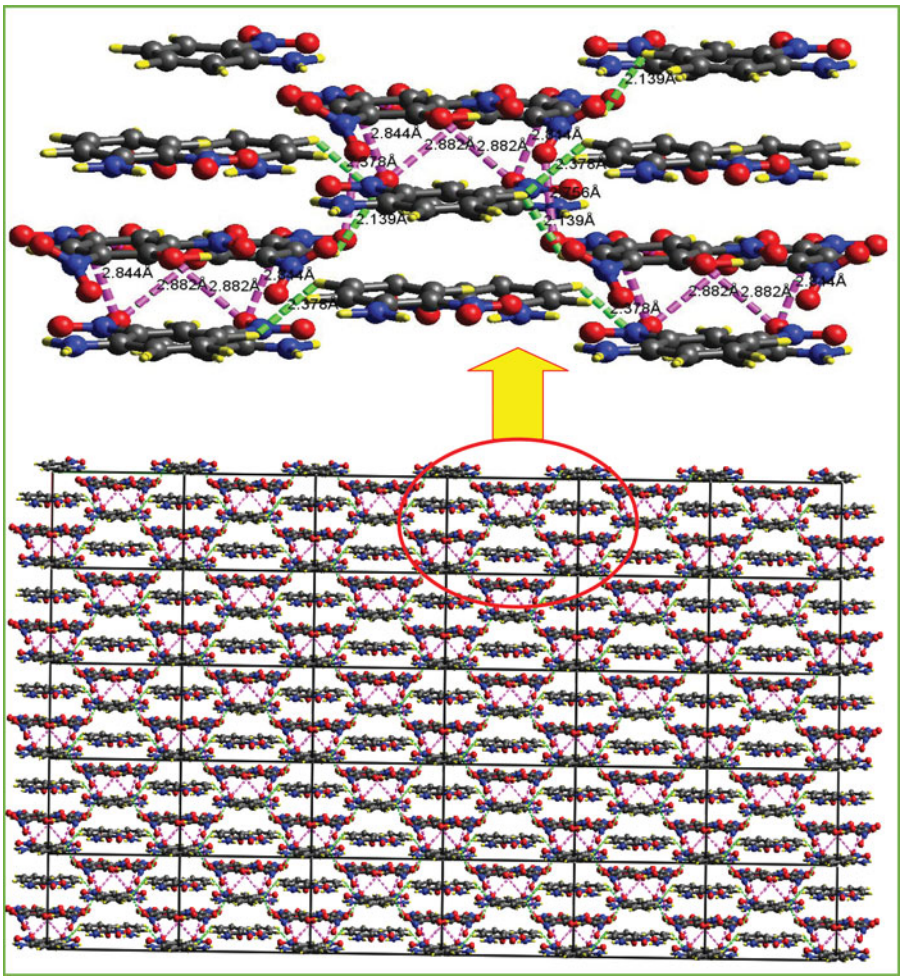

Figure 10. Packing projection along the *c*-axis showing H···H and O···O interactions.

where E_0 is the energy of the unperturbed molecule, F_α is the field of orgin, and μ_α, $\alpha_{\alpha\beta}$, and $\beta_{\alpha\beta\gamma}$ are the components of dipole moment, polarizability, and first-order molecular hyperpolarizability respectively,

$$\mu_0 = (\mu_x^2 + \mu_y^2 + \mu_z^2)^{1/2} \text{and}$$

$$\beta_0 = (\beta_x^2 + \beta_y^2 + \beta_z^2)^{1/2}.$$

$$\beta_x = (\beta_{xxx} + \beta_{xyy} + \beta_{xzz}),$$

$$\beta_y = (\beta_{yyy} + \beta_{xxy} + \beta yzz), \text{ and}$$

$$\beta_z = (\beta_{zzz} + \beta_{xxz} + \beta yyz).$$

Table 2. The calculated β components, β_{tot} value (esu), dipole moment (μ, D), and HOMO–LUMO (eV) characteristic of BNP.

β_{xxx}	−1581.083313
β_{xxy}	− 283.5798236
β_{xyy}	− 179.0038747
β_{yyy}	409.6047864
β_{xxz}	− 151.9292624
β_{xyz}	− 28.822792
β_{yyz}	− 243.4129021
β_{xzz}	− 37.2103288
β_{yxx}	− 317.6528709
β_{zzz}	− 16.7377441
β_{tot} ($\times 10^{-30}$)	16.01608199
μ	5.92
E_{HOMO}	− 7.215 *eV*
E_{LUMO}	− 4.122 *eV*
$E_{HOMO} - E_{LUMO}$	3.093 *eV*

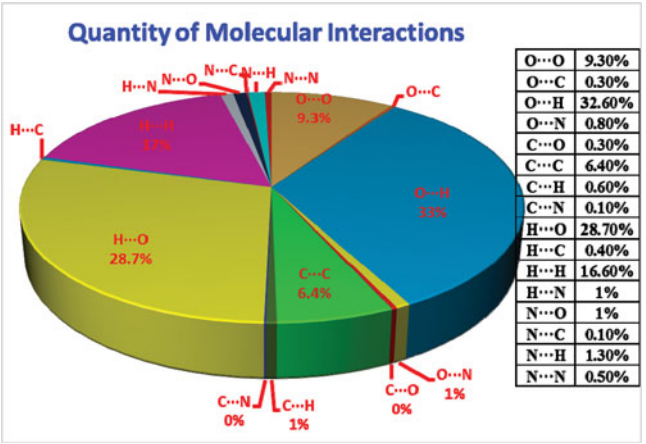

Figure 11. Pie chart of molecular interactions.

The computed first-order molecular hyperpolarizability (β) and dipole moment (μ) of the sample are 16.016 × 10^{-30} esu (>56.64 times of urea) and 5.92 D respectively (Table 2). A large β is due to the performance of non-zero μ values. High β rate is a required property of an NLO material.

Experimentally, NLO property is measured by using the Kurtz and Perry technique. The input beam energy is 2.82 mJ/pulse. Potassium Dihydrogen Phosphate (KDP) sample was used as a reference material ($I_{2\omega}$ = ~55 mV) and the powder Second Harmonic Generation (SHG) efficiency of BNP was found to be ~1.2 times that of KDP ($I_{2\omega}$ = ~66 mV).

3.6. *Hirshfeld surface analysis*

The Hirshfeld surface [32,33] is an essential approach for investigating intermolecular interactions. All the molecular interactions occurring in the crystal packing are quantified, and the pie chart of molecular interactions is displayed in Fig. 11. The Hirshfeld surface surrounding a molecule is indicated by points where the connection to the electron density from the molecule is identical to the influence from all other molecules. The normalized contact

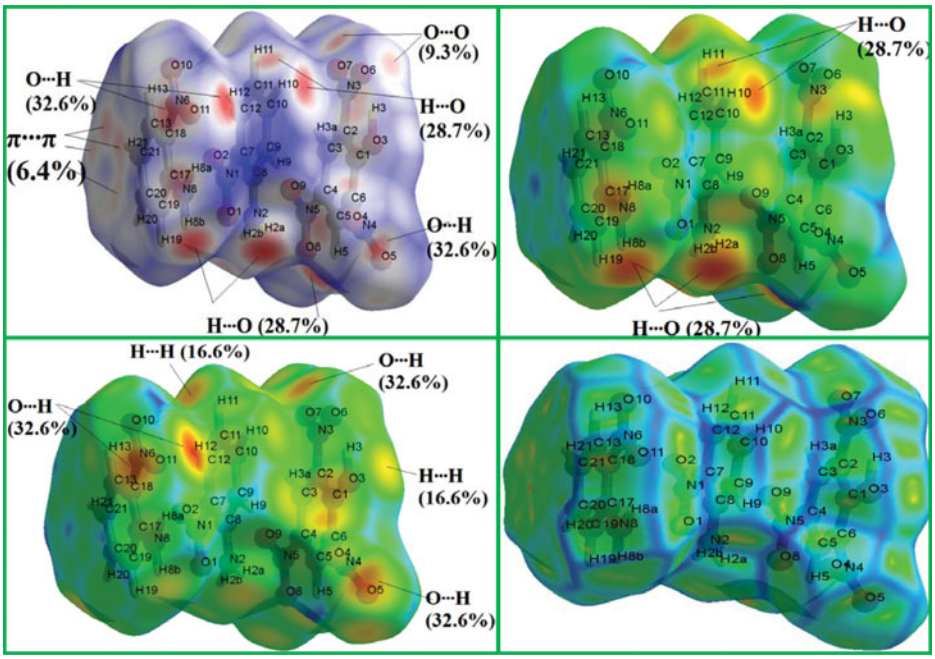

Figure 12. Hirshfeld surfaces of BNP: (a) *dnorm*, (b) *di*, (c) *de*, and (d) *curvedness*,

distance (*dnorm*) is based on both *de* and *di*, and the radii of the atom facilitate identification of the areas of specific intermolecular interactions. On behalf of every value on the isosurface, two distances are well defined, such as *de*-, the distance from the point to the adjacent nucleus external to the surface, and *di*-, the distance to the adjacent nucleus internal to the surface.

The value of the *dnorm* is negative or positive when intermolecular contacts are shorter or longer. Because of the symmetry between *de* and *di* in the appearance of *dnorm*, where two Hirshfeld surfaces touch, both will display a red spot identical in color intensity as well as size and shape. The combination of *de* and *di* in the form of a 2D fingerprint plot provides an immediate of intermolecular interactions in the crystal. Graphical plots of the molecular Hirshfeld surfaces were mapped with *dnorm* using a red–white–blue color system. The red indicates less distance interaction, white is comparatively long distance around the surface, and blue represents longer interactions. Moreover, further colored properties (curvedness, Fig. 12(d)) based on the local curvature of the surface can be specified.

Curvedness is the evaluation of "shape," while areas of sharp curvature possess a high curvedness and tend to divide the surface into patches associated with contacts between neighboring molecules. Bright red color in Fig. 12(a) is the indication of strong interactions such as O···O (9.3%), H···O (28.7%), $\pi \cdots \pi$ (6.4%), and O···H (32.6%). In the same way, *di surface* (Fig. 12c) indicates comparatively strong interactions O···H (32.6%). Weak interactions are indicated by yellow color in Fig. 12b, *de* surface clearly indicates the H···O (28.7%) interactions. Moreover, fingerprint plots [34] are a strong proof for the quantity of interactions with each and every molecule to molecule in crystal packing. Many interactions are symbolized as spikes in fingerprint plots (Fig. 13). The O···H, H···O, and H···H interactions are more. Less interactions are H···C and C···H (1%), N···O and O···N (1.5%), and O···C and C···O (0.6%).

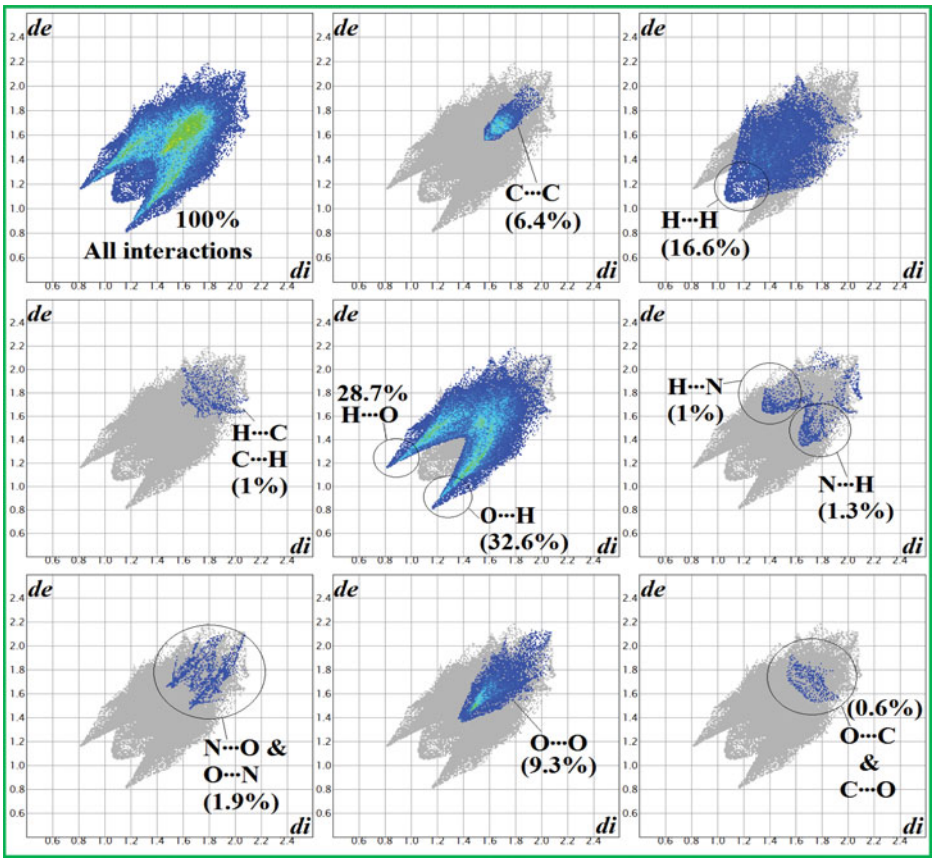

Figure 13. Fingerprint plot analysis of BNP.

4. Conclusions

Reddish yellow color crystals of BNP were successfully grown by slow evaporation solution growth technique at constant temperature. The product formation was confirmed by FT-IR and single crystal XRD analysis. Comparison of bond length and angles of theoretical and experimental values shows slight variations. It crystallizes in a space group *Cc* with four molecules in the unit cell. Hydrogen bonding interactions were quantified using fingerprint and Hirshfeld surface analysis. Supramolecular architecture is confirmed by inter- and intramolecular hydrogen bonding interactions were construed, and crystal cohesion was architectured by N-H···O, O-H···O, C-H···N, H···H, O···O, and $\pi\cdots\pi$ staking interactions.

Supplementary Data

CCDC1009556 contains the supplementary crystallographic data for this paper. These data can be obtained free of charge from The Cambridge Crystallographic Data Centre via www.ccdc.cam.ac.uk/data request/cif.

References

[1] Skarp, K., & Handschy, M. A. (1988). *Mol. Cryst. Liq. Cryst., 165*, 439–509.
[2] Moulson, A. J., & Herbert, J. M. (2003). *Electroceramics: Materials, Properties, Applications*, John Wiley: Chichester, UK.

[3] Senge Bymathias, O., Fazekas, M., Notaras Eleni, G. A., Blau Werner, J., Zawadzka, M., Locos Oliver, B., & Ni Mhuircheartaigh, E. M. (2007). *Adv. Mater.*, *19*, 2737–2774.
[4] Dhanabal, T., Amirthaganesan, G., & Dhandapani, M. (2014). *Optik*, *125*, 4341–4346.
[5] Lekshmi, P. N., Bijini, B. R., Prasanna, S., Eapen, S. M., Nair, C. M. K., Deepa, M., & Rajendra Babu, K. (2015). *Spectrochimica Acta A*, *137*, 778–784.
[6] Pansuriya Pramod, B., Maguire Glenn, E. M., & Friedrich Holger, B. (2015). *Spectrochimica Acta A, 142*, 311–319.
[7] Uma, J., & Rajendran, V. (2014). *Optik*, *125*, 816–819.
[8] Peramaiyan, G., Pandi, P., & Mohan Kumar, R. (2015). *J. Therm. Anal. Calorim.*, *119*, 291–299.
[9] Krishna Kumar, V., & Nagalakshmi, R. (2007). *Spectrochimica Acta A*, *66*, 924–934.
[10] Muthu, K., & Subbiah, M. (2012). *J.. Cryst. Growth*, *352*, 163–166.
[11] Aditya Prasad, A., Muthu, K., Meenatchi, V., Rajasekar, M., Meenakshisundaram, SP., & Mojumdar, S. C. J. (2015). *Therm. Anal. Calorim., 119*, 885–890.
[12] Aditya Prasad, A., Muthu, K., Rajasekar, M., Meenatchi, V., & Meenakshisundaram, SP. (2015). *Spectrochim. Acta A*, *135*, 46–54.
[13] Aditya Prasad, A., Muthu, K., Rajasekar, M., Meenatchi, V., & Meenakshisundaram, SP. (2015). *Spectrochim. Acta A*, *135*, 805–813.
[14] Frisch, M. J., Trucks, G. W., Schlegel, H. B., Scuseria, G. E., Robb, M. A., et al. (2009). *Gaussian 09, Revision C.01*, Gaussian: Wallingford, CT.
[15] Dennington, R., Keith, T., & Millam, J. (2009). *GaussView, Version 5*, Semichem: Shawnee Mission, KS.
[16] Jamroz, M. H. (2013). Vibrational energy distribution analysis, *Spectrochim. Acta A*, *114*, 220.
[17] Wolff, S. K., Grimwood, D. J., McKinnon, J. J., Jayatilaka, D., & Spackman, M. A. (2007). *Crystal Explorer 3.1*, University of Western Australia: Perth, Australia.
[18] Dolomanov, O. V., Bourhis, L. J., Gildea, R. J, Howard, J. A. K., & Puschmann, H. (2009). *J. Appl. Cryst.*, *42*, 339–341.
[19] Bourhis, L. J., Dolomanov, O. V., Gildea, R. J., Howard, J. A. K., & Puschmann, H. (2015). *Acta Cryst.*, *A71*, 59–75.
[20] Kurtz, S. K., & Perry, T. T. (1968). *J. Appl. Phys. 39*, 3798.
[21] Bharathikannan, R., Chandramohan, A., Kandhaswamy, M. A., Chandrasekaran, J., Renganathan, R., & Kandavelu, V. (2008). *Cryst. Res. Technol.*, *43*, 683–688.
[22] Mulliken, R. S. (1952). *J. Am. Chem. Soc.*, *74*, 811.
[23] Mulliken, R. S. (1955). *J. Chem. Phys.*, *23*, 1833.
[24] Maiorov, V. N., & Crippen, G. M. (1994). *J. Mol. Biol.*, *235*, 625–635.
[25] Hyndman, Rob J., & Koehler, Anne B. (2006). *Int. J. Forecast.*, *22*, 679–688.
[26] Thanthiriwatte, K. S., & Nalin de Silva, K. M. (2002). *J. Mol. Struct.*, *617*, 169.
[27] Liyange, P. S., de Silva, R. M., & Nalin de Silva, K. M. (2003). *J. Mol. Struct.*, *639*, 195.
[28] Koopmans, T. (1934). *Physica*, *1*, 104–113.
[29] Kubelka, P. (1948). *J. Opt. Soc. Am.*, *38*, 448.
[30] Saminathan, K., & Sivakumar, K., (2007). *Acta Cryst.*, *E63*, O354–O356.
[31] Kleinman, D. A. (1962). *Phys. Rev.*, *126*, 1977–1979.
[32] Hirshfeld, F. L. (1977). *Theor. Chim. Acta*, *44*, 129–138.
[33] Koenderink, J. J., & van Doorn, A. (1992). *Image Vision Comput.*, *10*, 557.
[34] Spackman, M. A., & McKinnon, J. J. (2002). *Cryst. Eng. Comm.*, *4*, 378.